New Journal of Physics
The open access journal at the forefront of physics
Deutsche Physikalische Gesellschaft DPG | IOP Institute of Physics

Directional absorption by phased arrays of plasmonic nanoantennae probed with time-reversed Fourier microscopy

Gabriel Lozano[1,3], **Tommy Barten**[1], **Grzegorz Grzela**[1] **and Jaime Gómez Rivas**[1,2]

[1] Center for Nanophotonics, FOM Institute AMOLF, c/o Philips Research, High Tech Campus 4, 5656-AE, Eindhoven, The Netherlands
[2] COBRA Research Institute, Eindhoven University of Technology, Eindhoven, The Netherlands
E-mail: lozano@amolf.nl

Received 16 October 2013, revised 20 December 2013
Accepted for publication 23 December 2013
Published 23 January 2014
New Journal of Physics **16** (2014) 013040
doi:10.1088/1367-2630/16/1/013040

Abstract

We demonstrate that an ordered array of aluminum nanopyramids, behaving as a phased array of optical antennae, strongly modifies light absorption in thin layers of dye molecules. Photoluminescence measurements as a function of the illumination angle are performed using a time-reversed Fourier microscope. This technique enables a variable-angle plane-wave illumination of nanostructures in a microscope-based setup. Our measurements reveal an enhancement of the light conversion in certain directions of illumination, which indicate the efficient diffractive coupling between the free space radiation and the surface plasmons. Numerical simulations confirm that surface modes supported by the periodic array enhance the intensity of the pump field in the space between particles, where the dye molecules are located, yielding a directional plasmonic-mediated enhancement of the optical absorption. This combined experimental and numerical characterization of the angular dependence of light absorption in nanostructures can be beneficial for the design and optimization of devices in which the harvesting of light plays a major role.

[3] Author to whom any correspondence should be addressed.

1. Introduction

Tailoring the optical absorption using nanostructures is a main goal for several research areas such as photovoltaics, sensing or photodetection [1–3]. Through the excitation of plasmonic resonances, i.e. the coherent oscillation of free electrons in metals driven by an external optical field [4], isolated metallic nanoparticles are capable of producing a high confinement and local field enhancement of the incident light, offering unprecedented possibilities for the interaction of light with matter at the nanoscale [5].

Light propagation in metallic nanostructured surfaces has been intensively investigated since the pioneering works of Wood and Fano [6, 7], offering a playground to yield remarkable optical phenomena [8, 9]. The radiative coupling between metallic particles arranged in a periodic array leads to collective modes, known as surface lattice resonances (SLRs) [10], which strongly depend on the size, shape and permittivity of the nanoparticles [11], as well as on the geometry and the dielectric environment of the lattice [12, 13]. The hybrid plasmonic–photonic nature of SLRs results in a spatial distribution of the electric field enhancement that extends away from the metal in the medium in which the nanoparticles are embedded. SLRs in metallic arrays were first described in the context of surface-enhanced Raman scattering [11, 14] and have been accurately characterized during the last few years [15–20].

In the particular case of light emission, plasmonic resonances are capable of modifying strongly the emission of nanosources [21]. Excited emitters located in the proximity of an array can decay into SLRs, that radiate into free space, allowing the control of spontaneous and stimulated emission [22, 23]. The extended field associated to SLRs allows overcoming the well-known limitation of the critical placement of the emitter relative to the metal nanoparticles in order to strongly modify the emission [24]. This system behaves as a phased array of optical antennae in which the radiation pattern of subwavelength sources is modified by the coherent scattering of the periodically spaced nanoparticles. The coupling of light emitters to SLRs yields a source with an increased spatial coherence. A very efficient outcoupling of the emission within narrow angular windows can be attained, enabling the beaming of the emitted light in specific directions [25]. This allows obtaining a collective enhancement of the emission from large volumes [26] in defined directions as it has been recently demonstrated in the context of solid-state lighting [27]. By reciprocity, the absorption of an ensemble of randomly distributed emitters should be enhanced for specific angles of illumination using a periodic array of metallic nanoparticles behaving as a receiving antenna.

In this paper, we demonstrate experimentally a strong angular-dependent optical absorption of dye molecules excited by means of phased arrays of optical antennae using time-reversed Fourier microscopy (TRFM). Fourier microscopy (FM) allows the characterization of the directionality of the emission from light sources sited in the vicinity of nanophotonic structures [28–33]. A microscope objective decomposes the incident light into plane waves and focuses each of them on distinct points of the back focal plane (BFP) of the objective lens. FM relies on imaging the BFP typically using a camera as a detector. An image of the BFP, thus, represents a projection of the reciprocal space on the plane of the camera and the intensity collected by each pixel in the camera is proportional to the emission intensity of the light source in a particular direction. In a TRFM the optical paths are time-reversed, which enables an angle-controlled plane wave illumination of a nanostructure investigated using a microscope objective. Herein we measure a square array of aluminum nanoparticles with the shape of nanopyramids on which a dye-doped polystyrene layer is deposited. The dimensions

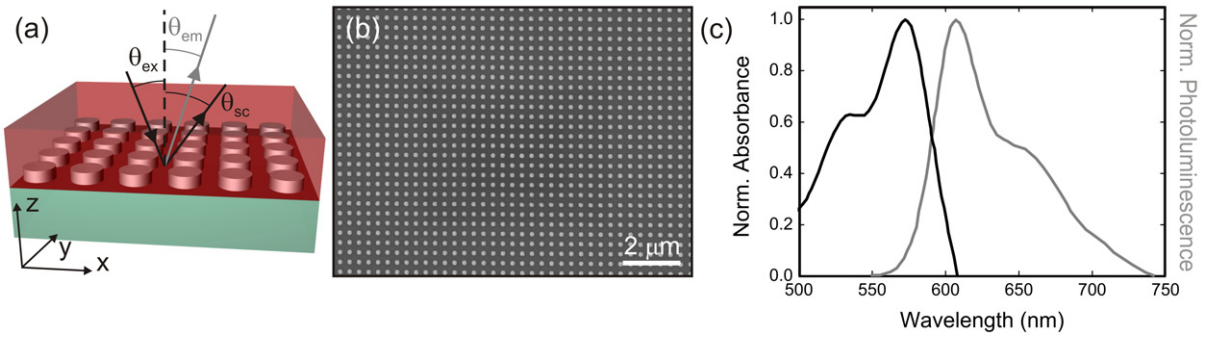

Figure 1. (a) A schematic representation of the aluminum nanoparticle array covered by a dye-doped polymer layer. Relevant angles, i.e., the elevation angles of illumination (θ_{ex}), emission (θ_{em}) and scattering (θ_{sc}), are signaled. (b) Scanning electron microscope image of a top view of the array of aluminum nanopyramids. Scale bar represents 2 μm. (c) Normalized absorbance (black) and PL (gray) spectra of the red dye.

of the aluminum nanoparticles and the geometry of the array have been designed such that the structure supports SLRs at the frequency of the excitation of the dye. SLRs enable a very efficient coupling between free-space radiation and localized surface plasmons which gives rise to a large enhancement of the optical near-field that extends into the surroundings of the nanoparticles, where the emitters are located. We will demonstrate that this effect is highly directional because of the dispersive character of the SLRs which renders the system into a receiving phased array of optical antennae. Numerical simulations will confirm that the coupling of the pump light to the collective modes supported by the array leads to an enhanced optical absorption in the emitting layer for defined directions of illumination. Finally, we will show that the enhancement of the optical pump field at 532 nm yields an overall fivefold emission enhancement when the plasmonic array is illuminated at 5.5° from the sample normal with p-polarized light.

2. Aluminum nanopyramid array

A schematic representation of the investigated structure is shown in figure 1(a). Aluminum nanopyramids, 140 nm in diameter at their base and 80 nm at their top, and 140 nm in height, arranged in a square array with lattice constant $a = 340$ nm were fabricated using substrate conformal imprint lithography in combination with reactive ion etching [34]. A scanning electron microscope image of a top view of such array is displayed in figure 1(b). The array is fabricated on top of a fused silica substrate. Aluminum supports plasmon resonances in the blue-to-ultraviolet region of the electromagnetic spectrum. In contrast to silver, aluminum self-passivates which facilitates its processing. The combination of aluminum and nanoimprint technology allows the fabrication of nanometer-precision replicas of plasmonic nanostructures over large areas using standard and inexpensive processes [27]. However, only very recently aluminum has been regarded as a plasmonic material [27, 35, 36]. A 250 nm-thick polystyrene layer containing dye molecules of Lumogen F Red 305 (BASF) at a concentration of 3 wt%, was applied by spin coating over the aluminum nanoparticles. The normalized absorbance and emission spectra of the dye are shown in figure 1(c). This red dye is characterized by a bright photoluminescence (PL) in the red part of the optical spectrum, a large stability and a high PL quantum yield which makes it highly interesting for solid-state lighting applications.

In order to understand the plasmonic resonances of the array, we have first simulated the response of an individual aluminum nanopyramid and an array of them. Three-dimensional electromagnetic simulations were performed with the finite-difference in time-domain method (FDTD).[4] To simplify the analysis, the nanoparticles are considered to be embedded in a homogeneous medium with a refractive index of 1.46. Figure 2(a) presents the scattering cross section (σ_{sc}) as a function of the free-space wavelength for an isolated aluminum nanopyramid (dashed black curve) and the extinction spectrum, which is defined as one minus transmittance (T), calculated at normal incidence when the nanoparticle is part of a square array (solid gray curve) with $a = 340$ nm. Several features may be noted in figure 2(a). Firstly, the scattering cross section of the isolated nanoparticle displays two distinct broad plasmonic resonances centered at 423 and 571 nm. Secondly, an extra feature is observed when the nanoparticles are arranged in a periodic lattice: a very sharp and intense peak emerges in the extinction spectrum in the long wavelength tail of the higher-energy resonance and close to the Rayleigh anomaly (RA), i.e. the onset of diffraction, of the $(\pm 1, 0)$ and $(0, \pm 1)$ diffracted orders (indicated by a vertical red-dashed line), which are degenerated at normal incidence.

To further assign the origin of the spectral features associated to the different plasmonic resonances, in figures 2(b)–(f), simulations of the spatial distribution of the intensity enhancement (IE)—i.e., total electric near-field intensity normalized by the incident intensity—are shown. Figures 2(b) and (c) display the IE calculated for an isolated nanoparticle at 423 and 571 nm, respectively. The field intensity is enhanced in the proximity of the nanoparticle, as expected for a localized surface plasmon polariton. The height of the nanoparticle and its tapering modify the distribution of the local field intensity around the nanoparticle. The intensity is more concentrated at the top of the nanopyramid for the resonance at 423 nm than for the resonance at 571 nm, whose field intensity is mainly concentrated in the base of the nanoparticle. The blue-shift of the 423 nm resonance compared to the one at 571 nm, is consistent with the higher field intensity in the top of the nanoparticle which is slightly smaller in size than the base of the nanoparticle. Figures 2(d)–(f) present the spatial distribution of the electric near-field intensity enhancement for the array of aluminum nanoparticles at three different wavelengths: 385, 502 and 565 nm, respectively. We consider a plane wave incident normal to the array. Numerical simulations reveal that the broad peaks in extinction observed at 385 and 565 nm can be associated to the localized resonances in the top and in the base of the aluminum nanoparticle, respectively. The simulation of the spatial intensity profile at 502 nm, presented in figure 2(e), shows a drastic redistribution of the near-field intensity with an enhancement that extends away from the

[4] FDTD Solutions (Lumerical Solutions Inc.) www.lumerical.com/. In order to calculate the scattering cross section of the individual nanopyramid, a simulation box size of $1 \times 1 \times 1\ \mu m^3$ with perfectly matched layer conditions on every boundary was used. The light source was a broadband (350–750 nm) plane wave, with normal incidence to the substrate. The mesh grid was set to 5 nm over the entire simulation volume, with a refinement of 1 nm over the volume occupied by the nanoparticle. The total-field scattered-field method was used to directly calculate the scattered power by means of frequency-domain transmission monitors positioned in the scattered field region. A two-dimensional frequency-domain field monitor cross-cutting the nanoparticle in its center was used to calculate the spatial distribution of the local electric field intensity. In order to calculate the transmittance of the periodic array, the box size was equal to $a \times a \times 1\ \mu m$ and periodic boundary conditions were used in the in-plane directions. The transmittance spectra was directly calculated with a frequency-domain transmission monitor. To calculate the spatial distribution of the local electric field intensity, a three-dimensional frequency-domain field monitor and a three-dimensional refractive index monitor that contain both the layer of refractive index 1.59 and the metallic nanoparticle were employed. The optical constants of Al were taken from [37].

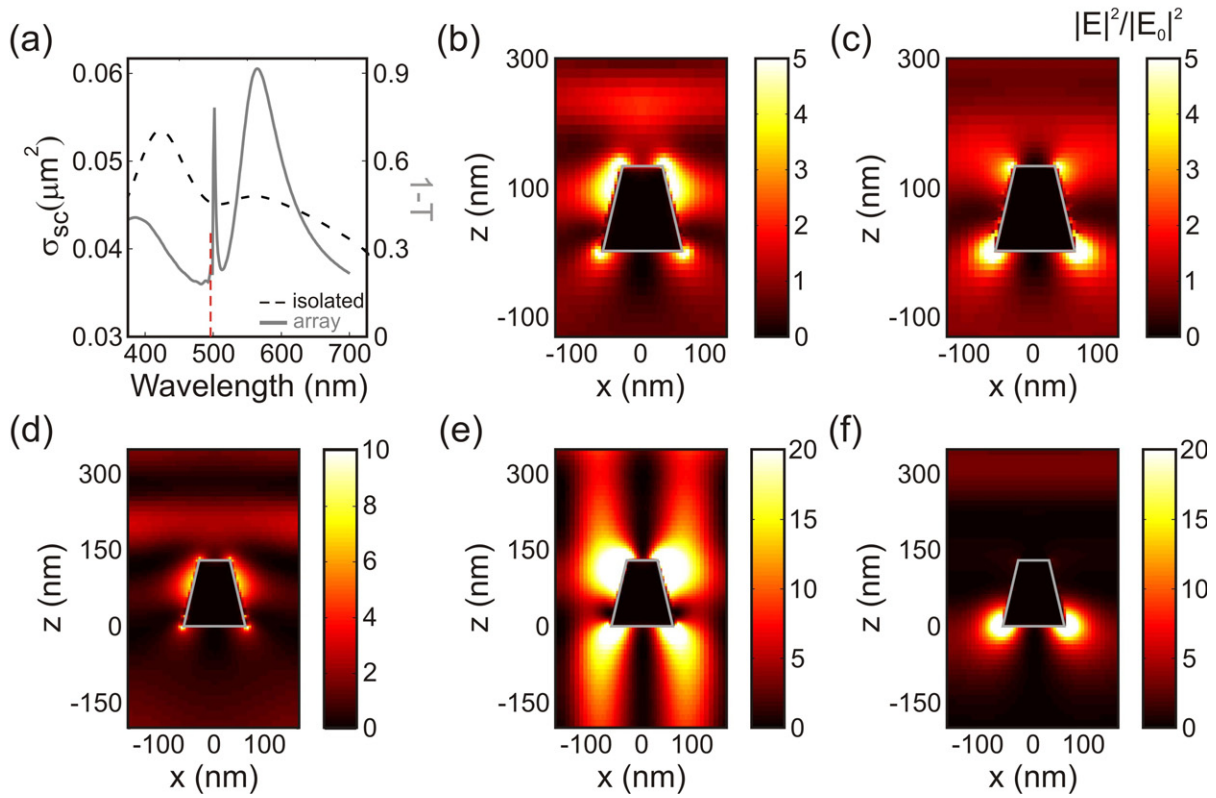

Figure 2. (a) FDTD simulations of the scattering cross section (σ_{sc}) spectra of an aluminum nanopyramid embedded in a homogeneous medium with a refractive index of 1.46 (dashed black curve). FDTD simulated extinction spectrum at normal incidence of the same nanopyramids ordered in a square array with a lattice constant of 340 nm (gray curve). The red dashed line corresponds to the Rayleigh anomaly calculated for the $(\pm 1, 0)$ and $(0, \pm 1)$ beams diffracted in a medium with a refractive index of 1.46. (b), (c) FDTD simulations of the spatial distribution of the total electric field intensity enhancement for the isolated nanoparticle at a wavelength of (b) 423 nm and (c) 571 nm. The color plot indicates the total electric field intensity ($|E^2|$) normalized to the incident intensity ($|E_0^2|$) on the plane intersecting the nanoparticles at $y = 0$. (d)–(f) FDTD simulated spatial distribution of the total electric field intensity enhancement ($|E^2|/|E_0^2|$) for an square array of the nanoparticles simulated in (a). The simulations consider a plane wave incident normal to the array with a wavelength of (d) 385 nm, (e) 502 nm and (f) 565 nm. The color plot indicates the intensity enhancement on the plane intersecting the nanoparticles at $y = 0$ in a unit cell of the array. The nanopyramids are outlined using gray curves.

nanoparticle in the surrounding medium. The sharp peak of high extinction, shown in figure 2(a) close to the RAs, originates from the coupling of localized surface plasmon polaritons supported by the individual nanopyramids to diffracted orders propagating in the plane of the array.

In the experiments, the particle array is not homogeneously surrounded by the same dielectric. The particles are on a fused silica substrate with a slightly lower refractive index (1.46) than the polystyrene layer (1.59), which is 250 nm thick. Figure 3(a) shows the extinction spectrum simulated for such system (gray curve) and compared with the measurement (black curve). The extinction spectrum was measured by illuminating the sample with the collimated

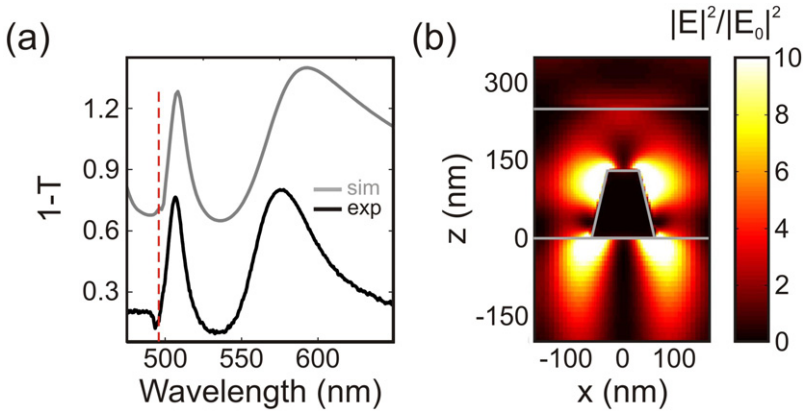

Figure 3. (a) FDTD simulated (gray curve) and measured (black curve) extinction spectra at normal incidence of a square array of aluminum nanopyramids with a lattice constant of 340 nm on a fused silica substrate and covered by a 250 nm thick dye-doped polymer layer. The red dashed line corresponds to the Rayleigh anomaly calculated for the $(\pm 1, 0)$ and $(0, \pm 1)$ beams diffracted in a medium with refractive index 1.46. (b) FDTD-simulated spatial distribution of the total electric field intensity enhancement ($|E^2|/|E_0^2|$) for the square array of the nanoparticles. The simulations consider a plane wave incident normal to the array with a wavelength of 508 nm. The color plot indicates the intensity enhancement on the plane intersecting the nanoparticles at $y = 0$ in a unit cell of the array. The nanoparticle and the different dielectric interfaces are outlined using gray lines.

beam from a halogen lamp at normal incidence. The intensity of the transmitted beam in the forward direction was collected using a fiber-coupled spectrometer. For the sake of clarity, the simulated extinction spectrum has been vertically shifted by 0.5 in figure 3(a). The main features in the measurements are reproduced in the simulations. The broad peak in extinction around 592 nm corresponds to the excitation of a plasmonic resonance in the aluminum nanopyramid, whereas the narrower resonance observed at 508 nm arises from the diffractive coupling of the nanoparticles in the square lattice. The spatial distribution of the IE simulated at 508 nm—see figure 3(b)—further confirms the collective nature of this mode with an IE that extends away from the nanopyramids both in the polymer layer and in the substrate. As it is demonstrated in what follows, light can couple very efficiently to these lattice-induced modes, enabling the effective coupling between far-field and near-field, which renders the periodic array in a receiving collective optical antenna. The delocalized and dispersive character of SLRs allows designing the interaction of these modes with light emitters sited in the proximity of the array such that a resonant enhancement of the optical absorption occur for specific directions of illumination.

3. Time-reversed Fourier microscopy

The principle of FM stems from the Fourier transformation properties of lenses. In a nutshell, imaging the BFP of a lens allows mapping the incoming wave field in the reciprocal space. For high numerical apperture (NA) and high-magnification objectives, the BFP is usually located within the body of the objective. Using an additional lens, the so-called Fourier lens, an enlarged image of the BFP, the so-called Fourier plane, can be created further away from the objective.

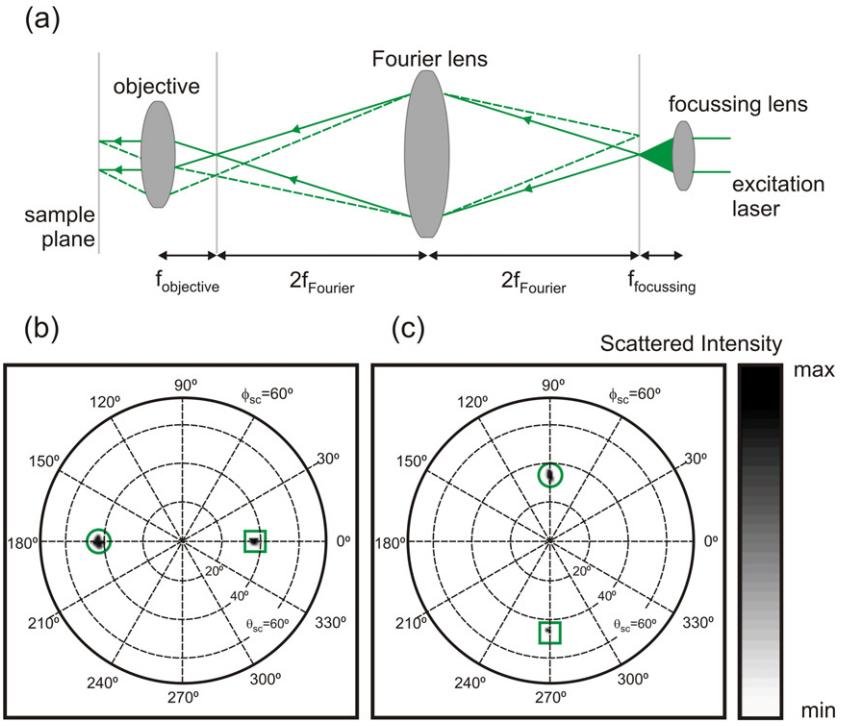

Figure 4. (a) Schematic respresentation of the working principle of a TRFM. (b), (c) Polar plot of the scattered intensity measured as a function of the scattered angle (θ_{sc}, ϕ_{sc}) from a square array of aluminum nanoparticles with 340 nm of lattice constant. The array is illuminated with a 450 nm laser source at an angle (b) $(\theta_{ex}, \phi_{ex}) = (45^\circ, 0^\circ)$ and (c) $(\theta_{ex}, \phi_{ex}) = (35^\circ, 270^\circ)$ using a TRFM. Calculated diffractive orders are indicated with open symbols. (0, 0), specular reflection, is signaled as an open circle and the $(-1, 0)$ and $(0, -1)$ orders as open squares in (b) and (c), respectively.

The concept of FM can be reversed by applying the reciprocity theorem [38]. In a TRFM, instead of imaging the BFP of the lens, a point source of monochromatic light can be generated in the BFP by focusing a laser beam to a spot in the Fourier plane. The emission of this point source is transmitted through the Fourier lens which transforms the spherical wavefronts into a plane wave. The direction of propagation of this plane wave ($\vec{k}$-vector) is determined by the location of the point source in the BFP. The accurate control over the position of this point in the BFP leads to a tailor-made plane-wave illumination of a nanostructure that is examined with a microscope objective. The so-called Fourier illumination achieved using a TRFM is schematically depicted in figure 4(a). TRFM offers the unique possibility of illuminating nanostructures with a well-defined wave vector using a microscope-based setup.

The level of accuracy of this optical tool can be tested by characterizing the diffraction displayed by the square array of aluminum nanoparticles shown in figure 1(b), and collected with a conventional FM when the array is illuminated using a TRFM. If a periodic lattice is shined with a plane wave, light will be diffracted into several beams that propagate in different directions. The conservation of the parallel component of the wave vector in the plane of the array leads to

$$\vec{k}_{\parallel sc} = \vec{k}_{\parallel ex} + p\vec{G}_x + q\vec{G}_y, \tag{1}$$

where $\vec{k}_{\parallel sc}$ and $\vec{k}_{\parallel ex}$ are the parallel components of the scattered and the incoming wave vectors and p and q are the two integers defining a particular diffracted order. For a square lattice, the reciprocal lattice vectors are given by $\vec{G}_x = \frac{2\pi}{a}\vec{e}_x$ and $\vec{G}_y = \frac{2\pi}{a}\vec{e}_y$ with $\vec{e}_x$ and $\vec{e}_y$ the unitary vectors along the x and y axes, respectively. Figures 4(b) and (c) show the Fourier images of the scattering from the sample when it is illuminated with $\lambda = 450\,\text{nm}$ laser light at two different angles, specifically $(\theta_{ex},\ \phi_{ex}) = (45^\circ,\ 0^\circ)$ and $(\theta_{ex},\ \phi_{ex}) = (35^\circ$ and $270^\circ)$, respectively. The Fourier images of the scattered intensity are recorded using a charge-coupled device camera and are plotted in polar coordinates, where the radius and the polar angle correspond, respectively, to the elevation (θ_{sc}) and the azimuthal (ϕ_{sc}) angle of the light scattered by the square lattice. The NA of the microscope objective determines the angular range in which the FM and the TRFM operate. In particular, a 0.95 NA microscope objective allows collecting light from the structure with large angles of scattering limited by a marginal ray at $\theta_{sc} = 72^\circ$ from the normal to the sample. Analogously, the maximum angle of illumination that can be attained using such objective with the TRFM is $\theta_{ex} = 72^\circ$. The position of the diffracted orders on the reciprocal space can be calculated according to equation (1). The calculated directions of the zeroth and first-order beams diffracted by the array are displayed as green open circles and squares, respectively. A good agreement between the measured and the calculated angular position of the different diffracted orders is attained.

4. Plasmonic-mediated directional enhanced absorption

In order to demonstrate the enhanced and angle-dependent optical absorption in the dye-doped polymer layer by the array of aluminum nanopyramids, PL measurements were performed using a TRFM. Notice that the time reversal refers to the optical technique rather than to the emission process itself. To quantify the improvement introduced by the plasmonic structure on the light absorption and emission, we define the PLE as the PL intensity measured from the emitting layer deposited over the array normalized by the PL of the same layer in the absence of the array. The PLE is measured for each angle of illumination $(\theta_{ex},\ \phi_{ex})$. The emitting layer is excited using a multimode continous wave $\lambda_{ex} = 532\,\text{nm}$ diode laser and the PL is collected by a 0.95 NA microscope objective and dispersed in a spectrometer.

In general, the PLE accounts for phenomena occurring at the excitation and at the emission frequencies of the randomly distributed dye molecules. Thus the PLE can be expressed as

$$\text{PLE}\,(\lambda_{ex},\,\Omega_{ex}) = \frac{\int_V H\,(\vec{r})\,|E\,(\vec{r},\,\lambda_{ex},\,\Omega_{ex})|^2\,,\,\mathrm{d}V}{\int_V H_{ref}\,(\vec{r})\,|E_{ref}\,(\vec{r},\,\lambda_{ex},\,\Omega_{ex})|^2\,\,\mathrm{d}V}, \tag{2}$$

where Ω_{ex} is the solid angle associated to the elevation and the azimuthal angle of excitation (θ_{ex}, ϕ_{ex}), $E(\vec{r}, \lambda_{ex}, \Omega_{ex})$ is the local field at the wavelength λ_{ex} and at the position $\vec{r}$ where each dye molecule is located that results from the illumination along Ω_{ex}. V is the volume of the emitting layer. $E_{ref}(\vec{r}, \lambda_{ex}, \Omega_{ex})$ corresponds to the local field in the absence of the nanoparticle array. The term $H\,(\vec{r})$ corresponds to the emission and can be expressed as

$$H\,(\vec{r}) = \int_{\lambda_{em}} \int_{\Omega_{em}} \eta\,(\vec{r},\,\lambda_{em},\,\Omega_{em})\;\mathrm{d}\lambda_{em}\,\mathrm{d}\Omega_{em}. \tag{3}$$

This term is due to the combined effect of (i) the local density of optical states at $\vec{r}$ to which an emitter can decay emitting radiation at the wavelength λ_{em}; and (ii) the outcoupling of this emission to free space radiation in the solid angle Ω_{em} associated to the elevation and the

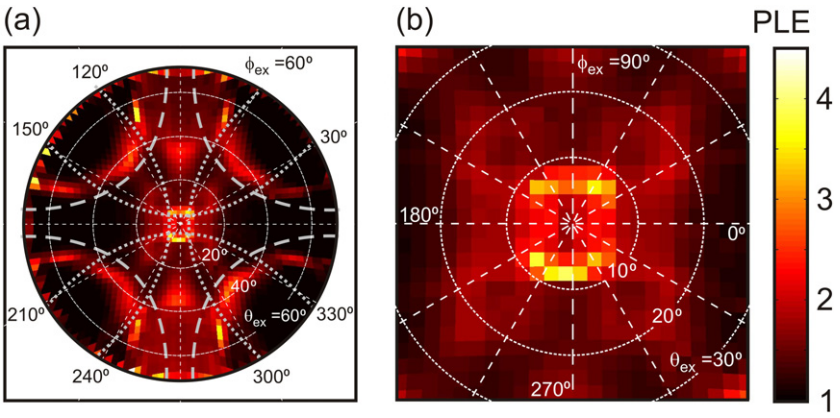

Figure 5. (a) PLE measured as a function of the illumination angle (θ_{ex}, ϕ_{ex}) from an array of aluminum nanopyramids on a fused silica substrate covered with a 250 nm-thick dye-doped polystyrene layer. The emitting layer is excited with a 532 nm laser using a time-reversed Fourier microscope. Results are displayed in polar coordinates, where the radius represents the elevation angle of excitation (θ_{ex}) and the polar angle corresponds to the azimuthal angle of excitation (ϕ_{ex}). Discontinous gray curves correspond to the Rayleigh anomalies calculated at a wavelength of 532 nm for the ($\pm$1,0), (0, $\pm$1) (dotted curves) and ($\pm$1, $\pm$1) (dashed curves) diffracted orders in a medium with a refractive index of 1.46. (b) Detail of (a) in the region close to $\theta_{ex} = 0$ deg where the largest PLE is found.

azimuthal angle of emission (θ_{em}, ϕ_{em}). $H_{ref}(\vec{r})$ represents the same physical quantity than $H(\vec{r})$ in the absence of the nanoparticle array. Note that both $H(\vec{r})$ and $H_{ref}(\vec{r})$ are assumed to be independent of Ω_{ex}. This assumption is not valid when $\lambda_{ex} = \lambda_{em}$. Therefore, the dependence of the PLE on the excitation angle is solely due to the local field intensity enhancement at the wavelength of excitation (λ_{ex}).

Figure 5(a) displays the PLE integrated throughout the emission spectrum of the dye (between 575 and 725 nm) as a function of the excitation angle (θ_{ex},ϕ_{ex}). Results are displayed in polar coordinates, where the radius represents the elevation angle of the excitation (θ_{ex}) and the polar angle corresponds to the azimuthal angle of the excitation (ϕ_{ex}). Due to the intrinsic polarization of the laser source, the incident light appears to be preferentially polarized along $\phi_{ex} = 90^\circ$ and 270°. This gives rise to the small asymmetry of the emission with a higher intensity along this direction of excitation. The measurements reveal a strong directional response with bands of enhanced PL that are associated to SLRs at the wavelength of excitation. The RAs are plotted as discontinuous gray curves in figure 5(a). Specifically, they correspond to the onset of ($\pm$1,0), (0, $\pm$1) and ($\pm$1, $\pm$1) diffracted orders, calculated at a wavelength of 532 nm, assuming that the array is embedded in a medium with a refractive index of 1.46. The coupling of the 532 nm light to these lattice-induced modes gives rise to narrow bands of enhanced directional light conversion that follow the dispersion of the SLRs, being slightly shifted from the RAs. Figure 5(b) shows that a 3.5-fold PLE is attained when the structure is pumped close to $\theta_{ex} = 5.5^\circ$ and $\phi_{ex} = 90^\circ$ or 270°.

Figure 6(a) shows the PLE as a function of θ_{ex} along $\phi_{ex} = 90^\circ$ using a $\lambda = 532$ nm laser source linearly polarized along this ϕ_{ex}. To ensure this polarization, a $\lambda/4$ plate and a linear polarizer were employed. Due to the orientation of the transmission axis of the polarizer, the excitation of the laser light is *p*-polarized along ϕ_{ex} and *s*-polarized along the orthogonal

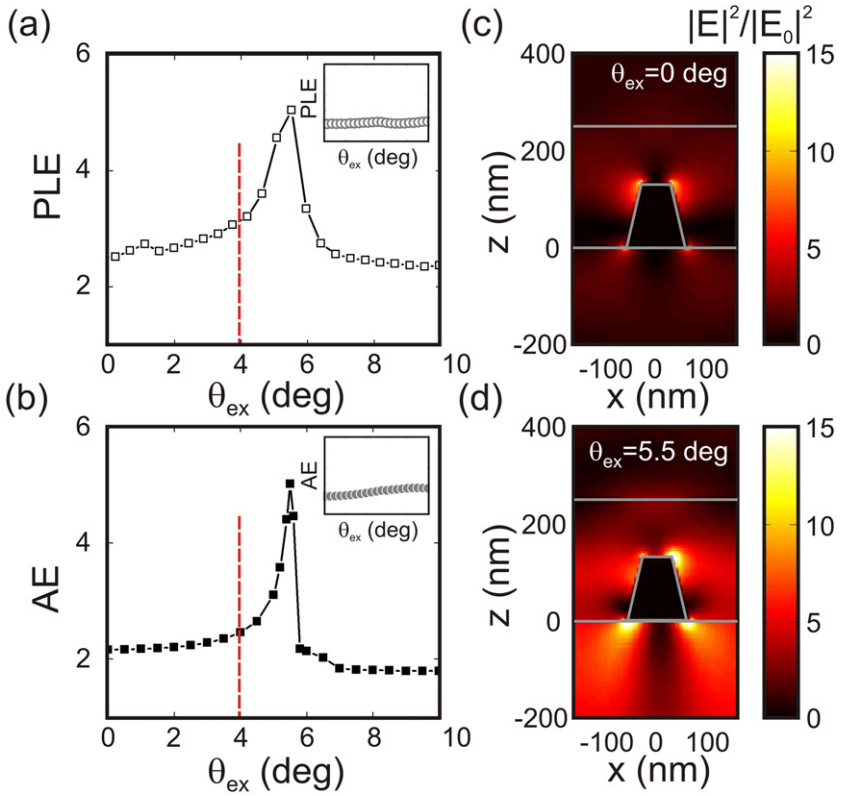

Figure 6. (a) PLE measured as a function of the excitation angle (θ_{ex}) along $\phi_{ex} = 90^\circ$ from an array of aluminum nanopyramids on a fused silica substrate covered with a 250 nm-thick dye-doped polystyrene. The emitting layer is excited with a p-polarized 532 nm laser source using a time-reversed Fourier microscope. The inset shows the result for s-polarized illumination. (b) FDTD simulated AE, i.e. the total electric field intensity integrated in a layer with a refractive index of 1.59 that covers an array of aluminum nanoparticles on a medium with refractive index of 1.46 normalized to the total electric field intensity integrated in the same layer deposited over the same medium in the absence of the metallic nanoparticles. The simulations consider a 532 nm p-polarized plane wave incident to the array forming an angle θ_{ex} with the z-axis. The inset shows the result for s-polarized illumination. The red dashed line in (a) and (b) correspond to the Rayleigh anomaly calculated for the (0,1) diffracted order in a medium with a refractive index of 1.46. (c, d) FDTD simulation of the spatial distribution of the intensity enhancement for a square array of aluminum nanopyramids on a medium with a refractive index of 1.46 covered by a 250 nm-thick layer of refractive index 1.59. The simulations consider a 532 nm p-polarized plane wave incident to the array forming an angle (c) $\theta_{ex} = 0^\circ$ and (d) $\theta_{ex} = 5.5^\circ$ with respect to the z-axis. The color plot indicates the intensity enhancement on the plane intersecting the nanoparticles at $y = 0$ in a unit cell of the array. The nanoparticle and the different dielectric interfaces are outlined using gray curves.

direction. A detailed explanation of the polarization analysis of FM can be found elsewhere [39]. A five-fold PLE is found when the emitting layer is excited at $\theta_{ex} = 5.5^\circ$ using a p-polarized wave. This remarkable pump enhancement attained from a large volume of emitting material using aluminum nanopyramids is attributed to a SLR associated to the (0,1) diffracted order. The dashed red line in figure 6(a) correspond to the RA calculated for the (0,1) beam diffracted in

a medium with a refractive index of 1.46. The enhancement is reduced when pumping off-resonance, being 2.5 at $\theta_{ex} = 0^\circ$. The PLE for s-polarized excitation, shown in the inset of figure 6(a), reaches a factor of 2.3 independently of θ_{ex} which shows that the SLR directional enhanced absorption is absent for s-polarization. The omnidirectional enhancement of the absorption of s-polarized light can be attributed to an increased scattering of the optical pump by the array. Out of resonance, the periodic array roughly behaves as a scattering mirror that increases the optical path of the pump field.

The absorption of the emitting layer, and consequently its PL, increases by the enhancement of the total electric near-field intensity at the pumping frequency in the regions of space where the dye molecules are located. Figure 6(b) displays the simulated absorption enhancement (AE), i.e., $|E(\vec{r}, \lambda_{ex}, \Omega_{ex})|^2$ integrated in the emitting layer over the nanoparticle array normalized by $|E_{ref}(\vec{r}, \lambda_{ex}, \Omega_{ex})|^2$, as a function of θ_{ex} for p-polarized 532 nm light. Simulations for s-polarized excitation are presented as an inset of figure 6(b). Note that good agreement is found between the PLE measurements and the AE simulations shown in figures 6(a) and (b), respectively. The spatial distribution of the IE simulated in the xz plane intersecting the particles at $y = 0$ in a unit cell of the array are displayed in figures 6(c) and (d) for $\theta_{ex} = 0^\circ$ and 5.5°, respectively. Figure 6(d) shows that, at resonance, the near-field intensity is enhanced throughout the emitting layer in the space between the aluminum nanopyramids. This intensity enhancement leads to the increase of the optical absorption in a volume of the dye layer larger than the typical associated to a localized plasmonic resonance. SLRs in phased arrays of optical antennae make dye-doped polymer layers deposited over periodic arrays of metallic nanoparticles efficient light converters at selected frequencies and angles.

5. Conclusions

The optical absorption of a thin layer of polymer containing dye molecules can be strongly enhanced using a periodic array of aluminum nanopyramids that behaves as a receiving phased array of optical antennae. Lattice-induced modes supported by such arrays, known as SLRs, yield an electric near-field intensity enhancement in the media surrounding the nanoparticles where the dye molecules are located. The collective and dispersive nature of SLRs enables an efficient coupling between the far-field illumination and the near-field excitation of the dye molecules that is angular selective. To investigate the directional enhanced optical absorption, TRFM was employed. This technique allows the illumination of nanostructures using a well-defined wave vector in a microscope-based setup. PL measurements as a function of the illumination angle reveal a fivefold emission enhancement for p-polarized light when the emitting layer is illuminated at a direction close to the sample normal. Numerical simulations confirm that the PLE originates from an enhanced optical absorption due to a near-field intensity enhancement mediated by the array of nanopyramids. These results may open new possibilities for the angular control and optimization of the optical absorption and light conversion in plasmonic-based devices. We envisage that TRFM will provide a wealth of new opportunities for the investigation of the angular dependence of light-matter interaction in nanostructures.

Acknowledgments

We thank M A Verschuuren and T Steinbusch for assistance in sample fabrication and S R K Rodriguez for stimulating discussions. This work is part of the research program of

the Foundation for Fundamental Research on Matter (FOM), which is financially supported by the Netherlands Organization for Fundamental Research (NWO). It is also part of an industrial partnership program between Philips and FOM. It is also supported in part by NanoNextNL, a micro and nanotechnology consortium of the Government of the Netherlands and 130 partners.

References

[1] Atwater H and Polman A 2010 Plasmonics for improved photovoltaic devices *Nature Mater.* **9** 205
[2] Offermans P, Schaafsma M C, Rodriguez S R K, Zhang Y, Crego-Calama M, Brongersma S H and Gómez Rivas J 2011 Universal scaling of the figure of merit of plasmonic sensors *ACS Nano* **5** 5151
[3] Knight M W, Sobhani H, Nordlander P and Halas N J 2011 Photodetection with active optical antennas *Science* **332** 702
[4] Raether H 1988 *Surface Plasmons on Smooth and Rough Surfaces and on Gratings* (*Springer Tracts in Modern Physics*) ed G Höhler and E A Niekisch (Berlin: Springer)
[5] Biagioni P, Huang J S and Hecht B 2012 Nanoantennas for visible and infrared radiation *Rep. Prog. Phys.* **75** 024402
[6] Wood R 1935 Anomalous diffraction gratings *Phys. Rev.* **48** 928
[7] Fano U 1941 The theory of anomalous diffraction gratings and of quasi-stationary waves on metallic surfaces (Sommerfelds waves) *J. Opt. Soc. Am.* **3** 213
[8] Ebbesen T W, Lezec H J, Ghaemi H F, Thio T and Wolff P A 1998 Extraordinary optical transmission through sub-wavelength hole arrays *Nature* **391** 667
[9] Pendry J B, Martín-Moreno and García-Vidal F J 2004 Mimicking surface plasmons with structured surfaces *Science* **305** 847
[10] García de Abajo F J 2007 Colloquium: light scattering by particle and hole arrays *Rev. Mod. Phys.* **79** 1267
[11] Kelly K L, Coronado E, Zhao L L and Schatz G C 2003 The optical properties of metal nanoparticles: the influence of size, shape and dielectric environment *J. Phys. Chem.* B **107** 668
[12] Bendaña X M and García de Abajo F J 2009 Confined collective excitations of self-standing and supported planar periodic particle arrays *Opt. Express* **17** 18826
[13] Rodriguez S R K, Abass A, Maes B, Janssen O T A, Vecchi G and Gómez Rivas J 2011 Coupling bright and dark plasmonic lattice resonances *Phys. Rev.* X **1** 021019
[14] Carron K T, Fluhr W, Meier M, Wokaun A and Lehman H W 1986 Resonances of two-dimensional particle gratings in surface-enhanced Raman scattering *J. Opt. Soc. Am.* B **3** 430
[15] Auguie B and Barnes W L 2008 Collective resonances in gold nanoparticle arrays *Phys. Rev. Lett.* **101** 143902
[16] Kravets V G, Schedin F and Grigorenko A N 2008 Extremely narrow plasmon resonances based on diffraction coupling of localized plasmons in arrays of metallic nanoparticles *Phys. Rev. Lett.* **101** 087403
[17] Chu Y, Schonbrun E, Yang T and Crozier K B 2008 Experimental observation of narrow surface plasmon resonances in gold nanoparticle arrays *Appl. Phys. Lett.* **93** 181108
[18] Vecchi G, Giannini V and Gómez Rivas J 2009 Surface modes in plasmonic crystals induced by diffractive coupling of nanoantennas *Phys. Rev.* B **80** 201401
[19] Zhou W and Odom T W 2011 Tunable subradiant lattice plasmons by out-of-plane dipolar interactions *Nature Nanotechnol.* **6** 423
[20] Evlyukhin A B, Reinhardt C, Zywietz U and Chichkov B N 2012 Collective resonances in metal nanoparticle arrays with dipole–quadrupole interactions *Phys. Rev.* B **85** 245411
[21] Muskens O L, Giannini V, Sánchez-Gil J A and Gómez Rivas J 2007 Strong enhancement of the radiative decay rate of emitters by single plasmonic nanoantennas *Nano Lett.* **7** 2871
[22] Vecchi G, Giannini V and Gómez Rivas J 2009 Shaping the fluorescent emission by lattice resonances in plasmonic crystals of nanoantennas *Phys. Rev. Lett.* **102** 146807
[23] Zhou W, Dridi M, Yong Suh J, Kim C H, Co D T, Wasielewski M R, Schatz G C and Odom T W 2013 Lasing action in strongly coupled plasmonic nanocavity arrays *Nature Nanotechnol.* **8** 506

[24] Anger P, Bharadwaj P and Novotny L 2006 Enhancement and quenching of single-molecule fluorescence *Phys. Rev. Lett.* **96** 113002
[25] Rodriguez S R K, Lozano G, Verschuuren M A, Gomes R, Lambert K, De Geyter B, Hassinen A, van Thourhout D, Hens Z and Gómez Rivas J 2012 Quantum rod emission coupled to plasmonic lattice resonances: a collective directional source of polarized light *Appl. Phys. Lett.* **100** 111103
[26] Pellegrini G, Mattei G and Mazzoldi P 2011 Nanoantenna arrays for large-area emission enhancement *J. Phys. Chem.* C **115** 24662–5
[27] Lozano G, Louwers D J, Rodriguez S R K, Murai S, Jansen O T A, Verschuuren M A and Gómez Rivas J 2013 Plasmonics for solid-state lighting: enhanced excitation and directional emission of highly efficient light sources *Light: Sci. Appl.* **2** e66
[28] Yoshita M, Koyama K, Baba M and Akiyama H 2002 Fourier imaging study of efficient near-field optical coupling in solid inmersion fluorescence microscopy *J. Appl. Phys.* **92** 862
[29] Gómez Rivas J, Vecchi G and Giannini V 2008 Surface plasmon polariton-mediated enhancement of the emission of dye molecules on metallic gratings *New J. Phys.* **10** 105007
[30] Curto A G, Volpe G, Taminiau T H, Kreuzer M P, Quidant R and van Hulst N F 2010 Unidirectional emission of a quantum dot coupled to a nanoantenna *Science* **329** 930
[31] Shegai T, Miljkovic V D, Bao K, Xu H, Nordlander P, Johansson P and Käll M 2011 Unidirectional broadband light emission from supported plasmonic nanowires *Nano Lett.* **11** 706
[32] Galisteo J F, López-García M, Blanco A and López C 2012 Studying light propagation in self-assembled hybrid photonic–plasmonic crystals by Fourier microscopy *Langmuir* **28** 9174
[33] Bernal Arango F, Kwadrin A and Koenderink A F 2012 Plasmonic antennas hybridized with dielectric waveguides *ACS Nano* **6** 10156
[34] Verschuuren M A 2010 Substrate conformal imprint lithographhy for nanophotonics *PhD Thesis* Utrecht University, The Netherlands
[35] Castro-López M, Brinks D, Sapienza R and van Hulst N F 2011 Aluminum for nonlinear plasmonics: resonance-driven polarized luminescence of Al, Ag and Au nanoantennas *Nano Lett.* **11** 4674
[36] Knight M W, Liu L, Wang Y, Brown L, Mukherjee S, King N S, Everitt H O, Norlander P and Halas N J 2012 Aluminum plasmonic nanoantennas *Nano Lett.* **12** 6000
[37] Palik E D 1985 *Handbook of Optical Constants of Solids* (New York: Academic)
[38] Born M and Wolf E 1997 *Principles of Optics* 6th edn (Cambridge: Cambridge University Press)
[39] Grzela G, Paniagua-Domínguez R, Barten T, Fontana Y, Sánchez-Gil J A and Gómez Rivas J 2012 Nanowire antenna emission *Nano Lett.* **12** 5481